The Astrophysical Journal, 719:655–670, 2010 August 10 doi:10.1088/0004-637X/719/1/655

MULTIWAVELENGTH IMAGING AND SPECTROSCOPY OF CHROMOSPHERIC EVAPORATION IN AN M-CLASS SOLAR FLARE

A. M. Veronig[1], J. Rybák[2], P. Gömöry[2,3], S. Berkebile-Stoiser[1], M. Temmer[1,4], W. Otruba[3], B. Vršnak[5], W. Pötzi[3], and D. Baumgartner[3]

[1] Institute of Physics, University of Graz, Universitätsplatz 5, A-8010 Graz, Austria; asv@igam.uni-graz.at
[2] Astronomical Institute, Slovak Academy of Sciences, SK-05960 Tatranská Lomnica, Slovakia
[3] Institute of Physics/Kanzelhöhe Observatory, University of Graz, A-9521 Treffen, Austria
[4] Space Research Institute, Austrian Academy of Sciences, Schmiedlstraße 6, A-8042 Graz, Austria
[5] Hvar Observatory, Faculty of Geodesy, Kačićeva 26, 1000 Zagreb, Croatia
Received 2010 February 16; accepted 2010 June 16; published 2010 July 22

ABSTRACT

We study spectroscopic observations of chromospheric evaporation mass flows in comparison with the energy input by electron beams derived from hard X-ray (HXR) data for the white-light M2.5 flare of 2006 July 6. The event was captured in high-cadence spectroscopic observing mode by *SOHO*/CDS combined with high-cadence imaging at various wavelengths in the visible, extreme ultraviolet, and X-ray domain during the joint observing campaign JOP171. During the flare peak, we observe downflows in the He I and O V lines formed in the chromosphere and transition region, respectively, and simultaneous upflows in the hot coronal Si XII line. The energy deposition rate by electron beams derived from *RHESSI* HXR observations is suggestive of explosive chromospheric evaporation, consistent with the observed plasma motions. However, for a later distinct X-ray burst, where the site of the strongest energy deposition is exactly located on the Coronal Diagnostics Spectrometer (CDS) slit, the situation is intriguing. The O V transition region line spectra show the evolution of double components, indicative of the superposition of a stationary plasma volume and upflowing plasma elements with high velocities (up to 280 km s^{-1}) in single CDS pixels on the flare ribbon. However, the energy input by electrons during this period is too small to drive explosive chromospheric evaporation. These unexpected findings indicate that the flaring transition region is much more dynamic, complex, and fine structured than is captured in single-loop hydrodynamic simulations.

Key words: Sun: chromosphere – Sun: corona – Sun: flares – Sun: transition region – Sun: UV radiation – Sun: X-rays, gamma rays

Online-only material: animations

1. INTRODUCTION

Solar flares are thought to be the result of magnetic reconnection in the corona, which releases vast amounts of energy within a few minutes (up to hours in the largest events). A substantial fraction of the released energy goes initially into the acceleration of suprathermal particles. Nonthermal electrons streaming down along the loops from a coronal acceleration region are stopped in the lower atmosphere due to the steep density increase in the transition region toward the chromosphere. There they deposit the bulk of their kinetic energy in Coulomb collisions with the ambient thermal electron population (Brown 1971; Lin & Hudson 1976). As a consequence of this energy input, the chromospheric plasma is strongly heated and expands upward, filling the coronal loops, which are then observed via their enhanced soft X-ray (SXR) and extreme ultraviolet (EUV) radiation. This process, known as "chromospheric evaporation," was first proposed by Neupert (1968) to explain the observed correlation between the thermal and cumulated nonthermal flare emission ("Neupert effect"; see, e.g., Dennis & Zarro 1993; Veronig et al. 2002).

Strongly blueshifted components and line asymmetries during the flare impulsive phase evidencing plasma upflows with speeds up to ~300–400 km s^{-1} have been first observed in spatially unresolved SXR spectroscopy from highly ionized ions formed at temperatures of 10^7 K with the Bent and Bragg Crystal Spectrometer (BCS) on board *Solar Maximum Mission* (*SMM*; e.g., Doschek et al. 1980; Antonucci et al. 1982; Zarro et al. 1988; Doschek 1990). Thereafter, flare-induced plasma flows were observed in SXR line spectra with *Yohkoh*/BCS (e.g., Culhane et al. 1993; Mariska et al. 1993; Bentley et al. 1994; Wuelser et al. 1994), and in spatially resolved EUV line spectra by *Solar and Heliospheric Observatory* (*SOHO*)/Coronal Diagnostics Spectrometer (CDS; e.g., Brosius 2003; Teriaca et al. 2003; Brosius & Phillips 2004; Kamio et al. 2005; Del Zanna et al. 2006; Milligan et al. 2006a). Hydrodynamic simulations of the atmospheric response to electron-beam heating confirmed that strong blueshifts in hot flare lines should be observed (e.g., Nagai & Emslie 1984; MacNeice et al. 1984; Fisher et al. 1985a, 1985b, 1985c; Allred et al. 2005; Liu et al. 2009). These models also predict a relation between the temperature and the expansion velocity of the evaporated plasma, which was recently confirmed from observations of a C-class flare with the EUV Imaging Spectrometer (EIS) on board *Hinode* covering a multitude of emission lines in the temperature range 0.05–16 MK (Milligan & Dennis 2009).

It is important to note that these one-dimensional single-loop models predict that in the early flare phase the total line profile should be blueshifted by several hundred kilometers per second, but the majority of the observations revealed only a blue asymmetry of the spectral lines indicating the presence of a strong static component (e.g., Doschek & Warren 2005, and references therein). However, the observations can be reconciled with the numerical simulations if a multi-thread fine structure of the flaring atmosphere is accounted for in the modeling (Hori et al. 1997; Warren & Doschek 2005; Doschek & Warren 2005). In the multi-loop scenario, chromospheric evaporation occurs sequentially in a number of individual threads that together make

up a larger loop system that may appear as a single loop in X-ray or EUV images. As a consequence, the integrated emission of the newly heated loops (subject to chromospheric evaporation plasma flows) and the previously heated loops (static) does not reveal bulk motions.

Important observational diagnostics of the energy input by electron beams is provided by their hard X-ray (HXR) radiation, assumed to be thick-target bremsstrahlung of electrons scattered off the ions when impinging on the chromosphere (Brown 1971). The bulk of the kinetic energy of the fast electrons is lost in Coulomb collisions with the ambient thermal electrons, which is efficiently heating the flaring chromosphere. Only a tiny fraction ($\sim 10^{-5}$) of the kinetic energy of the electrons is converted to HXR radiation when they are decelerated in the fields of the ions. However, it is the spatial and spectral distribution of this HXR bremsstrahlung which provides us with important insight into the acceleration, transport, and energetics of electron beams in solar flares.

Hydrodynamic simulations predict that depending on the incident energy flux, the atmosphere responds by one of two means (e.g., Fisher et al. 1985a, 1985b, 1985c; Mariska et al. 1989; Abbett & Hawley 1999a). If the energy deposition rate is too small to raise the chromospheric temperature beyond the peak of the radiative loss function at around 10^5 K, the pressure can be raised by no more than a factor of 10. In this case, the heated atmosphere moves slowly upward at several tens of kilometers per second to adjust to a new equilibrium position, so-called "gentle chromospheric evaporation." Gentle evaporation may also be due to thermal conduction from the hot flaring corona, and was observed in small flares as well as in the preflare and late phase of larger events (Czaykowska et al. 1999; Brosius & Phillips 2004; Milligan et al. 2006b). For high-energy flux densities ($\gtrsim 10^{10}$ erg cm^{-2} s^{-1}), the chromosphere is unable to radiate away the deposited energy at a sufficient rate and is rapidly heated to coronal temperatures. In this case, the pressure increases by at least a factor of 10^2 (up to 10^3). Consequently, the chromospheric plasma expands explosively upward into the loop at velocities of several hundred kilometers per second, in a process called "explosive chromospheric evaporation." The overpressure of the hot evaporating plasma relative to the underlying chromosphere pushes cooler, more dense material downward at velocities of several tens of kilometers per second, establishing momentum balance with the hot plasma upflows (e.g., Fisher et al. 1985a). Such momentum balance was deduced from some flare observations to within an order of magnitude (Zarro et al. 1988; Canfield et al. 1990; Teriaca et al. 2006). In a recent paper, Brosius (2009) studied the plasma flow behavior at different temperatures with CDS high-cadence spectroscopy and finds a change from explosive to gentle evaporation during the M1.5 flare in his investigation. This change from explosive to gentle evaporation could be due to the atmosphere being heated and filled with evaporated material during the earlier event. This would reduce the amount of electron beam flux reaching the chromosphere during the second event, since due to the increased column density a larger part of low-energy electrons is already stopped in the coronal part of the loop (Brosius 2009).

In this paper, we study a well-observed M2.5 flare that occurred on 2006 July 6, and concentrate on the flare-induced chromospheric evaporation mass flows observed by CDS, in comparison with the energy input by electron beams derived from HXR data and the results of hydrodynamic simulations. The flare was captured with high-cadence spectroscopy across the southern flare ribbon in UV and EUV emission lines by *SOHO*/CDS in combination with multi-wavelength high-cadence imaging of the photosphere (*Transition Region and Coronal Explorer* (*TRACE*) white light, *SOHO*/MDI white light and magnetograms), the chromosphere (*TRACE* UV, Kanzelhöhe and Hvar Hα), and transition region and corona (*TRACE* EUV). In addition, we also have *RHESSI* X-ray observations during the flare impulsive phase, which provide us with imaging and spectroscopy of the hot flaring plasma in the corona ($\gtrsim 10^7$ K) and allow us to deduce the energy input by flare-accelerated electron beams.

The paper is structured as follows. In Section 2, we give a detailed description of the various data and instruments involved in the study, and describe the co-alignment of the different data sets. In Section 3, we present an event overview and our results structured into multi-wavelength imaging, CDS spectroscopy, and *RHESSI* imaging and spectroscopy. In Section 4, we discuss our findings and how they relate to hydrodynamic simulations of the flaring atmosphere. Finally, we present our conclusions in Section 5.

2. DATA AND DATA REDUCTION

The flare observations analyzed in this paper were acquired during a coordinated observing campaign performed during 2006 June 28 to July 12. The *SOHO* Joint Observing Program JOP171 included the operation of *TRACE* (Handy et al. 1999), CDS (Harrison et al. 1995), and the Michelson Doppler Imager (MDI; Scherrer et al. 1995) on board *SOHO* (Domingo et al. 1995), as well as the ground-based Dutch Open Telescope on La Palma (DOT; Hammerschlag & Bettonvil 1998), the Hvar Observatory of the University of Zagreb (Croatia), and the Kanzelhöhe Observatory of the University of Graz (Austria).[6] On July 6, an M2.5 flare occurred at a heliographic position of (S09°, W34°) in the target field of view (FOV) of AR 10898, which was observed by all campaign instruments except DOT (due to bad weather conditions). For our study, we also use the HXR observations of the *Ramaty High Energy Solar Spectroscopic Imager* (*RHESSI*; Lin et al. 2002).

2.1. SOHO CDS, MDI, and EIT

During JOP171, the Normal Incidence Spectrometer (NIS) on CDS (Harrison et al. 1995) provided simultaneous high-cadence spectra of six EUV lines formed at chromospheric, transition region and coronal temperatures, used to determine spatially resolved intensities and line-of-sight flow speeds at flaring pixels. Emission lines of the following ions were selected, which we list together with their nominal wavelength and formation temperature (Landini & Monsignori Fossi 1990; Stucki et al. 2002): He I ($\lambda = 584.3$ Å, $T \sim 3.9 \times 10^4$ K), O III ($\lambda = 599.6$ Å, $T \sim 1.2 \times 10^5$ K), O V ($\lambda = 629.7$ Å, $T \sim 2.6 \times 10^5$ K), Ne VI ($\lambda = 562.8$ Å, $T \sim 4.2 \times 10^5$ K), Mg IX ($\lambda = 368.0$ Å, $T \sim 1.0 \times 10^6$ K), and Si XII ($\lambda = 520.7$ Å, $T \sim 2 \times 10^6$ K). The CDS slit covered an area of $2'' \times 140''$ with a pixel size of $2'' \times 1''.7$. The spatial resolution of CDS is larger than this, about $5''$–$6''$, due to the size of the point spread function (Pauluhn et al. 1999). During our observing campaign, the CDS slit was set fixed in a sit-and-stare mode (i.e., no compensation for solar rotation was applied) acquiring observations at a cadence of ~15 s (exposure time 10 s) during the period ~7:25 UT to 12:55 UT. Before and after the one-dimensional observing sequence,

[6] Further details on the campaign can be found at our JOP171 Web site: http://www.astro.sk/~choc/open/06_dot/06_dot.html

four raster scans of 20 successive steps of the CDS slit in the x-direction, corresponding to an area of $40'' \times 140''$, were obtained for co-alignment purposes. The CDS data were corrected for the CCD bias, deviations in exposure time, flat-field and cosmic ray hits using CDS standard calibration software available in the SolarSoftWare (SSW) tree.

CDS spectra acquired after the recovery of the *SOHO* spacecraft in 1998 are characterized by broad and asymmetric line profiles, and were fitted with a single broadened Gaussian component.[7] During the flare impulsive phase, the O V profiles in several pixels along the slit were composed of more than one component, and were hence fitted with a two-component broadened Gaussian model. The line fits provided the specific peak intensities, the wavelength positions of the core and the width of the line. The selected spectral lines all showed preflare and postflare components. Of particular interest for our study are the Doppler velocities of mass flows caused by the flare energy deposited in the chromosphere, which were calculated from the wavelength shift of the line centroid relative to its nominal wavelength. Positive velocities (redshifts) denote motions away from the observer, i.e., toward the solar surface; negative velocities (blueshifts) indicate motions upward into the corona. The quiet Sun shows characteristic flow patterns, in the transition region dominated by continuous redshifts. Since we are interested in the chromospheric evaporation flows induced by the flare energy release, we "compensate" for the continuous quiet Sun flows by determining the reference wavelength ("zero velocity") by averaging for each pixel the derived center wavelength position during the postflare phase 11:00–12:55 UT. We note that this procedure gives relative velocities (i.e., not absolutely calibrated). In this paper, we concentrate on the evolution in the He I, O V, and Si XII lines, which provide the best signal and cover the full temperature range from the chromosphere to corona. The 1σ uncertainties of the velocities are estimated to 5 km s^{-1} for He I, 10 km s^{-1} for O V, and 20 km s^{-1} for Si XII.

On 2006 July 6, we acquired a sequence of MDI full-disk line-of-sight magnetograms ($1\farcs96$ pixel^{-1}; Scherrer et al. 1995) with a cadence of 1 minute. Each hour, one MDI white-light image was also taken. For the global context of the event as well as for co-alignment purposes, we also used the EUV full-disk images acquired in the 304 Å (He II), 171 Å (Fe IX/X), and 195 Å (Fe XII/XXIV) filters by the Extreme-ultraviolet Imaging Telescope (*SOHO*/EIT; Delaboudinière et al. 1995). EIT observed with a time cadence of ∼12 minutes in the 195 Å passband and 6 hr in the other passbands, with a pixel resolution of $\sim 2\farcs6$. The CDS rasters were taken close in time to the EIT cycle through all four wavelengths, which is regularly done each 6 hr, to optimize the data co-alignment. Dark current and flat field were corrected using the EIT data reduction routines available in SSW.

2.2. TRACE

The *TRACE* satellite (Handy et al. 1999) provided image sequences in the 171 Å (Fe IX/X) passband, observing plasma at a temperature of $\sim 10^6$ K, with a cadence of ∼80 s. Each 10 minutes, we obtained a cycle of *TRACE* images at 1216 Å (hydrogen Lyα), 1600 Å (UV continuum), 1550 Å (C IV), and white light. The *TRACE* filtergrams feature the solar photosphere, chromosphere, transition region, and corona with a spatial sampling of $0\farcs5$ pixel^{-1} for a $\sim 511'' \times 511''$ FOV. We applied *TRACE* flat-fielding and dark current subtraction using the SSW *TRACE* data reduction routines. The effect of cosmic ray particle hits present in some *TRACE* images was reduced by median filtering.

2.3. RHESSI

RHESSI observes high-energy solar flare emission from 3 keV to 17 MeV with high spectral and spatial resolution for a full-Sun FOV (Lin et al. 2002). *RHESSI* uses a set of nine rotating modulation collimators consisting of pairs of widely separated X-ray opaque grids with high-sensitive Germanium detectors behind each collimator. The X-ray images of the source are reconstructed by ground-based software (Schwartz et al. 2002) from the incident photon fluxes, which are time modulated by the nine modulation collimators as the spacecraft rotates at 15 revolutions per minute (Hurford et al. 2002).

The impulsive phase of the M2.5 flare of 2006 July 6 was fully captured by *RHESSI* observations. We reconstructed *RHESSI* images in the 6–12 and 20–60 keV energy bands with the CLEAN algorithm using grids 3–8, giving a spatial resolution of $\sim 7''$ (Hurford et al. 2002). In the 6–12 keV band (dominated by thermal emission of plasma with temperatures $\gtrsim 10^7$ K), we reconstructed images for consecutive intervals of 30 s. In the 20–60 keV band (dominated by nonthermal emission of electron beams), we reconstructed images over individual bursts in the *RHESSI* high-energy light curves with integration intervals in the range 30–60 s. In addition, for the determination of footpoint source sizes, we also reconstructed *RHESSI* images over selected peaks in the 20–60 keV energy band with the Pixon and the MEM-NJIT algorithms using grids 1–8. Pixon and MEM-NJIT are suitable algorithms to provide reliable estimates of the reconstructed X-ray source sizes (Dennis & Pernak 2009). Note that for these image reconstructions during the HXR peaks, we also used the finest *RHESSI* grid no. 1 (only possible in the case of good count statistics), which has an FWHM angular resolution of $2\farcs3$. *RHESSI* spectra were extracted with 1 keV spectral resolution using all front detectors 1–9 except 2 and 7 (with lower spectral resolution and high threshold energies), deconvolved with the full detector response matrix (Smith et al. 2002) and fitted with an isothermal plus thick-target bremsstrahlung spectrum (Holman et al. 2003) for consecutive 12 s intervals throughout the flare impulsive phase.

2.4. Ground-based Hα Imaging

During JOP171, we acquired full-disk Hα images at Kanzelhöhe Observatory with a cadence of ∼3 s. The images have a spatial sampling of $2\farcs2$ pixel^{-1} and are tracked and aligned using a solar limb-finding algorithm (Otruba & Pötzi 2003). In addition, we acquired Hα filtergrams of AR 10898 at Hvar Observatory (Otruba 2005) with a cadence of ∼4 s. The Hvar Hα images cover an FOV of about $300'' \times 300''$ centered on the AR, and were co-aligned via cross-correlation techniques with Kanzelhöhe Hα images.

2.5. Data Co-alignment

Much care has to be taken in such an extensive multiwavelength study combining imaging and spectroscopic observations from various instruments, to properly co-align all the different data sets. Such considerations were already part of the planning of the JOP171 observing run. The co-alignment between different instruments was derived by the two-dimensional

[7] CDS software note Nr. 53: http://solar.bnsc.rl.ac.uk/swnotes/cds_swnote_53.pdf

cross-correlation of images or CDS raster scans sensitive to similar temperature ranges (showing similar atmospheric layers) and recorded close in time to each other. Generally, several pairs of images/scans were used for the cross-correlations, and a linear approximation of the shifts in time led to offsets of the coordinate systems with uncertainties typically below $\sim 1''$. The reference coordinate system for our data set was EIT, which has a pointing accuracy of $\sim 2''$. First, CDS He I 584 Å raster images were co-aligned with the EIT He II 304 Å full disk image, which was taken roughly at the same time. *TRACE* 171 Å maps were co-aligned with the EIT maps in the same wavelength band, and the pointing information was used to update all other *TRACE* filtergrams, accounting for the varying FOV of the individual *TRACE* filters. The co-aligned *TRACE* white-light images were the reference for the MDI full-disk white-light images, and the determined offsets were also applied to the MDI magnetograms. Kanzelhöhe full-disk Hα images were co-aligned with EIT 195 Å images of the active region. Hvar Hα maps were then co-aligned with the Kanzelhöhe Hα images. *RHESSI* has a pointing accuracy of better than $1''$, and the pointing information given in the image fits header was not altered. With the resulting co-alignment, brightenings along the CDS slit coincided well with bright flare kernels observed in Hα and in *TRACE* UV images, which further coincided with the *RHESSI* HXR footpoint emission observed at several time steps. We also quantified the errors in our co-alignment by repeating the procedure at different times and in changing the sequence of the instruments and filters. We estimate that the co-alignment for our data set is correct to within $\sim 2''$.

3. RESULTS

3.1. Event Overview and Context Observations

On 2006 July 6, the instruments involved in the JOP171 campaign pointed to AR 10898 located at 6° south and 34° west from the solar meridian. Figure 1 shows a full-disk white-light image and longitudinal magnetogram from *SOHO*/MDI together with an Hα filtergram from Kanzelhöhe Observatory taken directly before the onset of the M2.5 flare. Figure 2 shows a subfield around AR 10898 observed by MDI and the different *TRACE* passbands. The active region appears rather simple (Wilson classification β), with the negative polarity leading sunspot embedded in a network cell of predominantly positive polarity fields. The white-light image reveals two light bridges across the sunspot, the most prominent one crossing the spot in the north–south direction.

Figure 1 in Berkebile-Stoiser et al. (2009) shows a high-resolution view of AR 10898 obtained on 2006 July 4 with the Dutch Open Telescope in *G* band, Ca II H and Hα together with a high-resolution MDI magnetogram, a *TRACE* 171 Å, and a *TRACE* white-light frame. The MDI high-resolution magnetogram acquired on July 4 shows that the magnetic elements surrounding the sunspot are highly intermixed on small scales. It can also be seen that early on that day, the light bridge was not yet formed. It started forming later on the day of July 4, associated with a distinct anti-clockwise rotation of the sunspot between 2006 July 4 and 6. We note that AR 10898 did not produce flares above B-level from June 26, when it rotated over the eastern solar limb, until July 4. On July 4, it was the source of several microflares (studied in detail in Berkebile-Stoiser et al. 2009) and a C1-class flare. On July 5, it produced two C-class flares, increasing to its maximum flare activity on July 6, where it was the source of the M2.5 flare under study.

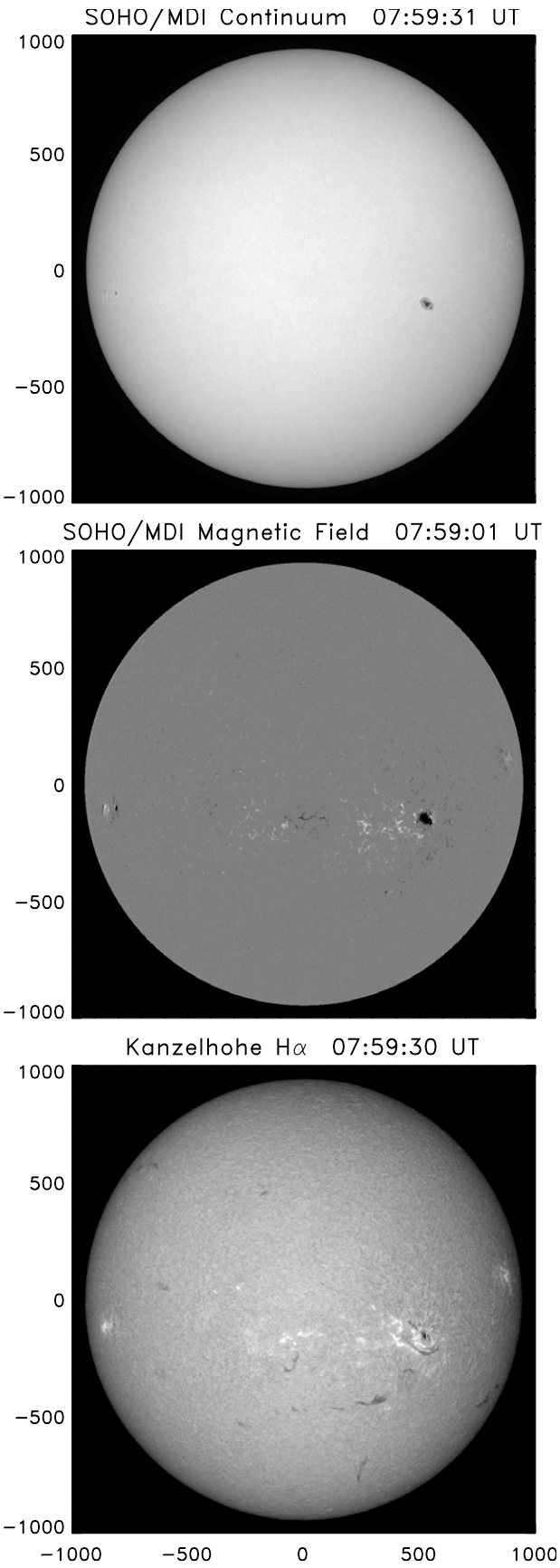

Figure 1. Overview of AR 10898 (S06, W34) on 2006 July 6, shortly before the start of the M2.5 flare. From top to bottom: *SOHO*/MDI continuum image, *SOHO*/MDI longitudinal magnetic field map, Kanzelhöhe Observatory Hα filtergram. The units on the *x*- and *y*-axes are in arcseconds; the same holds for all images plotted in the following.

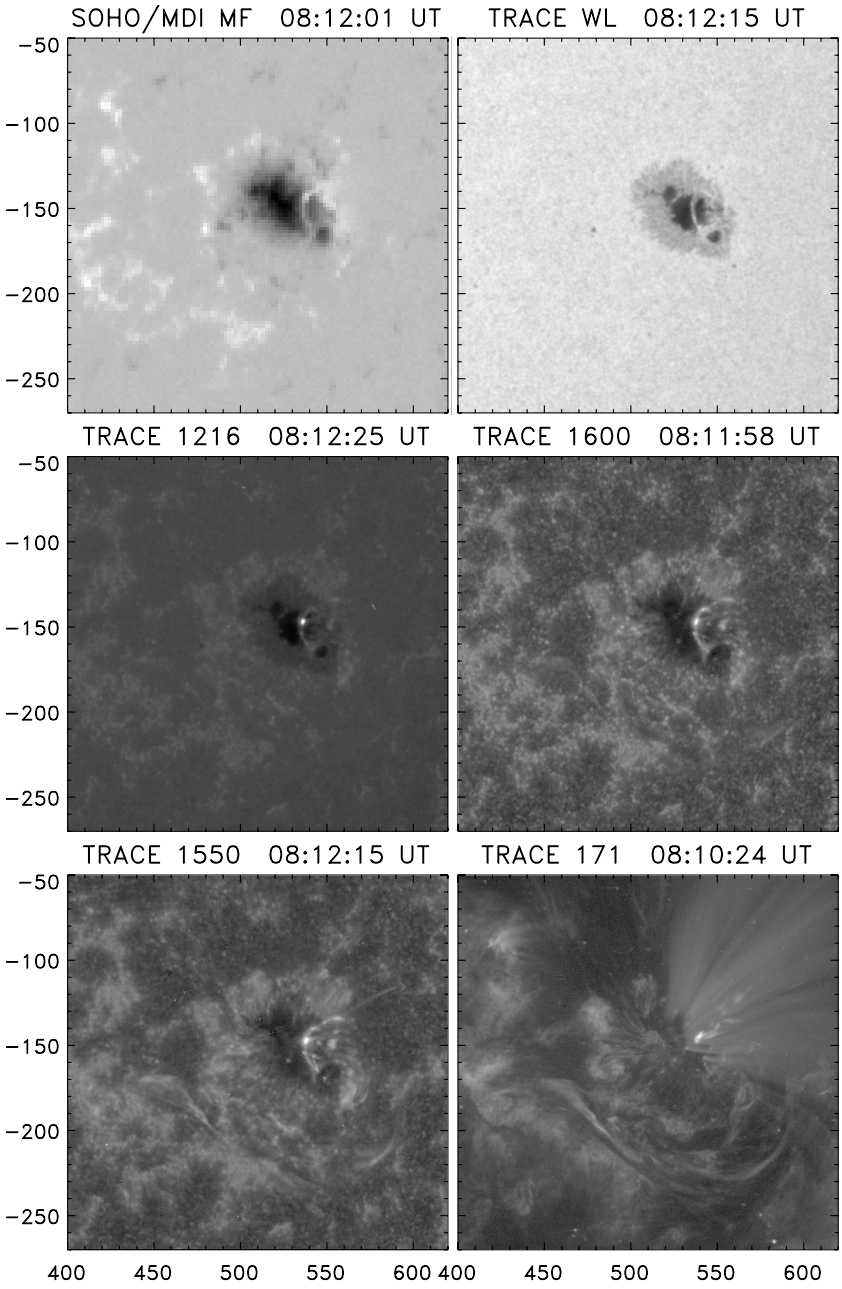

Figure 2. Multiwavelength imaging at the beginning of the flare: *SOHO*/MDI longitudinal magnetic field, *TRACE* white light, *TRACE* 1216, 1550, 1600, and 171 Å filtergrams. In the accompanying movie1, we show the evolution of the event in the *TRACE* 171 Å passband.

(An animation of this figure is available in the online journal.)

The M2.5 flare that occurred on 2006 July 6 around 8 UT was a textbook two-ribbon flare with associated filament eruption and coronal mass ejection (CME). The associated CME was fast ($\sim$900 km s^{-1} in the *SOHO*/LASCO coronagraph's FOV). Its main acceleration phase was studied in detail in Temmer et al. (2008), revealing a peak acceleration of 1.1 km s^{-2} around 08:20 UT. The event was accompanied by a propagating shock wave, as is evidenced by the coronal and interplanetary type II burst observations of the Astrophysikalisches Institut Potsdam (AIP) and Wind/WAVES dynamic radio spectra. Finally, we note that the event was associated with distinct, long-lasting bipolar coronal dimming regions (see movie1 for the evolution in *TRACE* 171 Å), which are generally interpreted as being due to mass depletion in the wake of the erupting CME and associated field line opening (e.g., Hudson et al. 1996; Zarro et al. 1999). The evolution of this dimming region was studied by several groups (McIntosh et al. 2007; Jiang et al. 2007; Attrill et al. 2008).

3.2. Multi-wavelength Imagery of the M2.5 Flare

The M2.5 flare of 2006 July 6 is preceded by activation of the AR filament (starting as early as 07:40 UT) and by distinct localized brightenings and mass flows in the sunspot light bridge observed in *TRACE* 1216, 1550, 1600, 171 Å and Hα images around 08:01 and 08:11 UT (see Figures 2 and 3). We note that continuous brightenings and associated mass flows in the light bridge can be observed during the overall JOP171 observing period on July 6 from 07:25 to 12:55 UT. The brightenings appear most pronounced in the *TRACE* Lyα 1216 Å spectral line (see Figure 4 and movie2). Light bridges are regions of

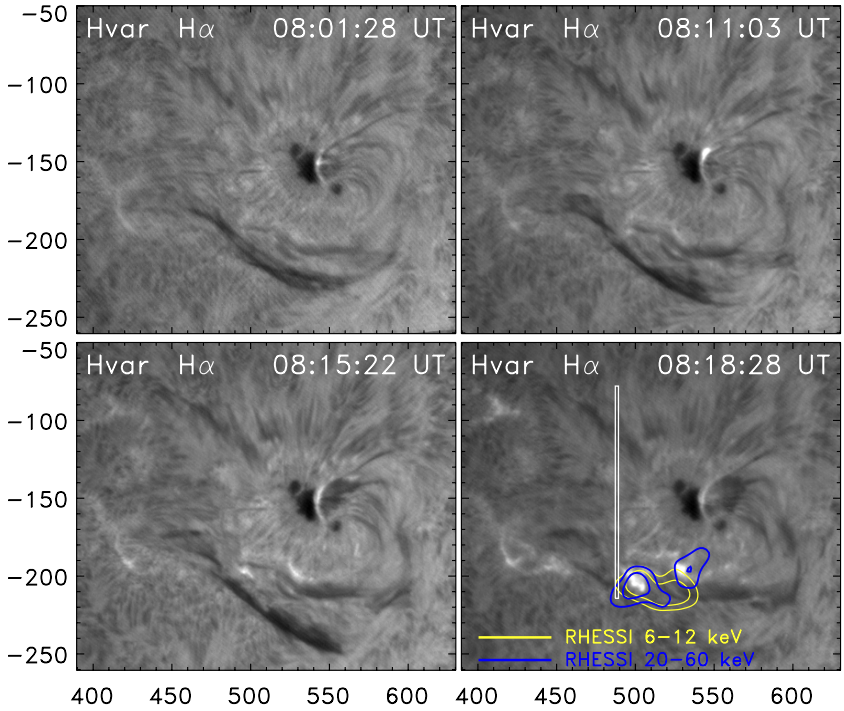

Figure 3. Early phase of the flare as observed in the Hα spectral line at Hvar Observatory. Note the brightenings in the light bridge (top panels) and associated mass flows from the light bridge (bottom panels). Yellow and blue contours in the last panel are *RHESSI* 6–12 keV (thermal) and 20–60 keV (nonthermal) flare radiation. The vertical rectangle indicates the position of the CDS slit.

strong magnetic field gradients within a sunspot, and may thus be favorable locations for current sheets and magnetic reconnection to occur (e.g., Rüedi et al. 1995; Leka 1997; Qiu et al. 2002). Recently, Shimizu et al. (2009) studied *Hinode*/Solar Optical Telescope high-resolution vector magnetic field measurements of a light bridge that produced recurrent chromospheric plasma ejections. These authors report the possible direct detection of electric currents flowing in the current sheet formed at the magnetic reconnection sites above the light bridge.

The impulsive phase of the M2.5 flare under study starts with two footpoint brightenings south of the main sunspot of AR 10898, observed in Hα and in *RHESSI* HXRs around 08:15–08:18 UT (Figure 3), which then develop to extended flare ribbons expanding in a north–south direction. In Figure 5, we show images obtained in the different *TRACE* passbands around the flare maximum. It can be seen that in its maximum phase, the flare is associated with distinct enhancements in white light at the southern flare ribbon. These white-light enhancements spatially coincide with the *RHESSI* 20–60 keV footpoint emission from flare-accelerated electrons.

In Figure 6, we show a sequence of the flare during the impulsive phase up to its decay phase observed in the *TRACE* 171 Å passband together with *RHESSI* 6–12 and 20–60 keV X-ray emission (see also online movie3). The 20–60 keV nonthermal HXR emission is located along the strongest brightenings of the *TRACE* flare ribbons. The 6–12 keV emission comes from the region between the *RHESSI* HXR footpoints, located above the *TRACE* postflare loops, evidencing hot plasma ($T \sim 20$ MK) from the rising flare loop system. In the accompanying movie3 one can see that the *TRACE* 171 Å ($T \sim 1$ MK) postflare loops first appear in the image at 08:35:50 UT, whereas the hot *RHESSI* flare loops can be observed already around 08:18 UT. This time difference of 18 minutes provides a rough estimate of how long it takes the hot flaring plasma to cool from about 20 MK to 1 MK, which is predominantly due to conductive cooling (cf. discussions in Vršnak et al. 2006).

3.3. CDS Spectroscopy

Figure 6 shows a sequence of *TRACE* 171 Å images together with the position of the CDS slit, revealing that the slit crosses the southern flare ribbon. Roughly 10 pixels along the lower end of the CDS slit are at some instant located directly at the flare ribbon, which moves southward as the flare progresses. In Figure 7, we plot a small *TRACE* 171 Å subfield around the southern flare ribbon together with the *RHESSI* 20–60 keV contours and the CDS slit, indicating the size of the individual CDS pixels. In Figure 8, we show the evolution in three selected pixels for the full CDS observing period. We plot the integrated intensity and the velocity derived from the one-component Gaussian fits to the CDS spectra in the He I, O V, and Si XII lines. The 1σ uncertainties of the velocity calibration derived from the CDS spectra in the postflare phase are indicated by horizontal lines.

Figure 8 reveals three distinct periods with upflows observed in the O V line. The first two peaks, around 07:45–08:05 UT and 08:15–08:20 UT are related to the activation and eruption of the AR filament. This can be best confirmed and followed in the online movie4, where we combine the imaging information from *TRACE* 171 Å images with integrated intensities and velocities observed in O V along the CDS slit. Figure 9 shows three snapshots of this movie. The top panel is taken during the time of filament lift-off and the commencement of the impulsive flare phase. It reveals blueshifts in the pixels covering the rising filaments, and redshifts (due to chromospheric evaporation downflows) in the pixels covering the bright flare footpoints. We also note that at some instants during the filament activation and lift-off several CDS pixels covering the eruption appear redshifted (see movie4). This may be an effect of internal motion

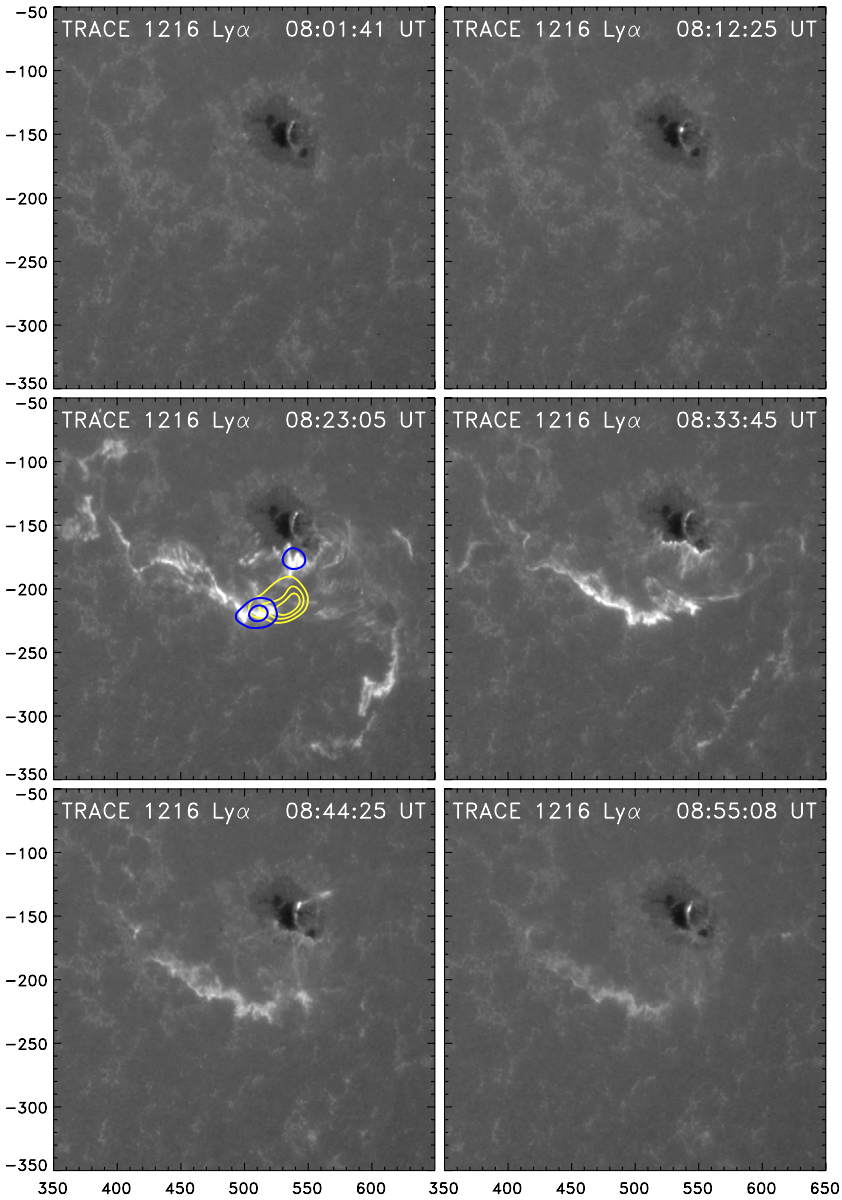

Figure 4. Evolution of the flare and the brightenings in the sunspot's light bridge as observed in *TRACE* 1216 Å hydrogen Lyα spectral line from 08:01 to 08:55 UT. Images are logarithmically scaled. The contours in the third panel are co-temporal *RHESSI* 20–60 keV (blue: 30% and 70% of the image's maximum) and 6–12 keV emission (yellow: 40%, 60, and 80% of the image's maximum). In the accompanying movie2, the full time range from 07:50 to 12:50 UT is presented, showing the ongoing brightenings and activations in the light bridge, before, during, and after the flare.

(An animation of this figure is available in the online journal.)

of the filament (twisting) while it rises. The filament lift-off is observed in all three spectral lines during 08:15–08:20 UT with line-of-sight velocities in the CDS FOV up to 40–60 km s^{-1}, indicating the multithermal nature of the erupting filament plasma covering a broad temperature range from $\sim 10^4$ up to at least 2×10^6 K.

Figure 10 shows the CDS spectroscopy results together with the *RHESSI* X-ray flux at different energy bands for the flare impulsive phase. The integrated intensities in He I and O V show impulsive behavior with a sequence of distinct peaks (with a typical duration of $\sim$1 minute), whereas the Si XII intensities show only one peak around 08:21 UT, coincident with peaks in He I and O V, but a gradual increase thereafter. It is worth noting that the intensity peaks observed in adjacent CDS pixels do not necessarily occur at the same time and with the same strength, due to the flare spatial/temporal evolution along the CDS slit. A similar argument holds when we compare the CDS intensities in the chromospheric (He I) and transition region lines (O V) with the *RHESSI* HXR flux: the peaks are somehow related but do not occur simultaneously. This can be explained by the fact that in the *RHESSI* light curves we observe the spatially integrated X-ray flux, whereas in the CDS light curves constructed for individual pixels, we see the emission from a certain small ($2'' \times 1\farcs7$) subfield of the flaring region at a certain instant.

The strongest HXR peaks occur between 08:20 and 08:26 UT, with the increase of the nonthermal emission ($\gtrsim$20 keV) starting already around 08:18 UT (see also the top panel in Figure 10). We note that during this period, the CDS slit is not directly located on the site of strongest energy deposition as evidenced by the *RHESSI* HXR footpoints but crosses the flare ribbon slightly to the east of the HXR footpoints (cf. Figures 5 and 6). During this period, we also observe a sequence of strong peaks

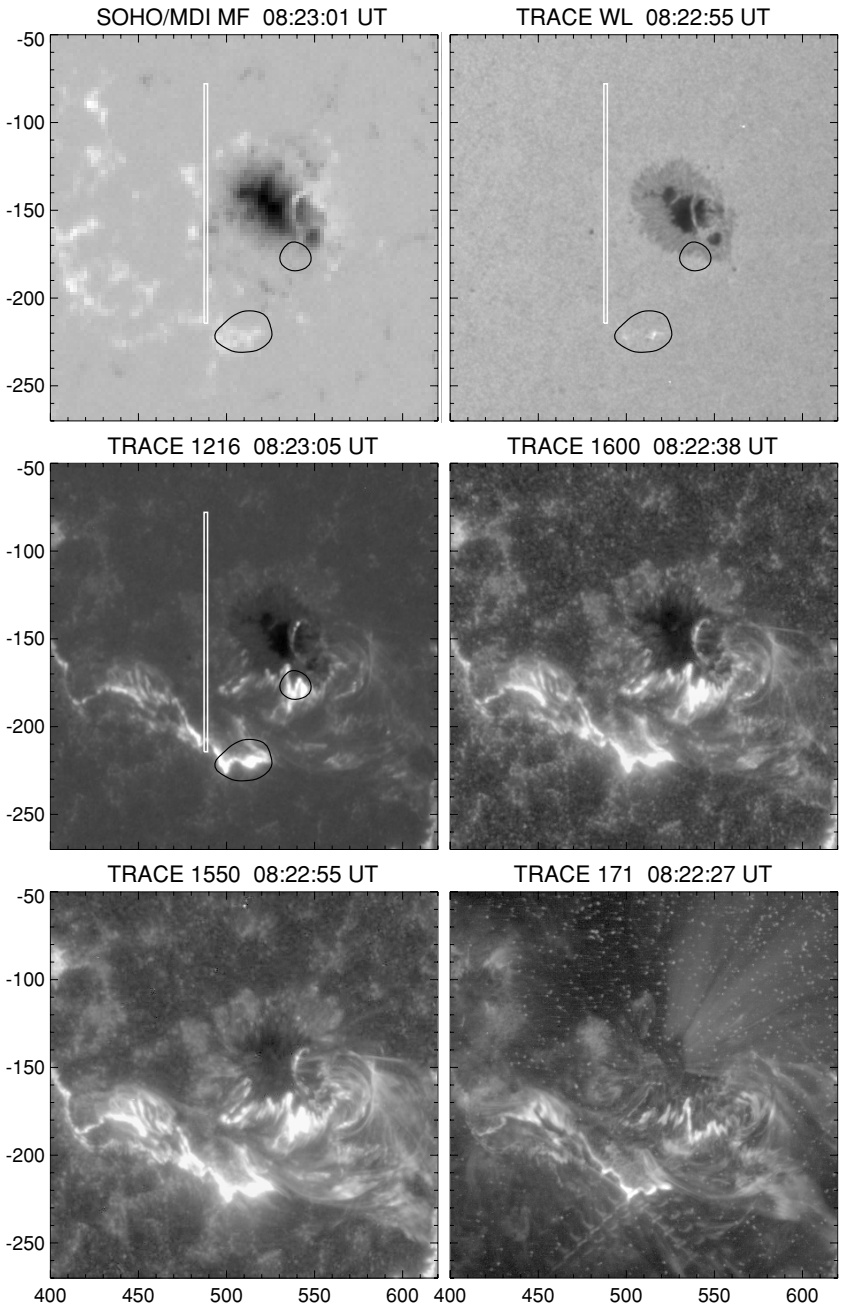

Figure 5. Multiwavelength imaging during the flare maximum: *SOHO*/MDI longitudinal magnetic field, *TRACE* white light, *TRACE* 1216, 1550, 1600, and 171 Å filtergrams. The white rectangle outlines the CDS slit. The contours indicate the contemporaneous *RHESSI* 20–60 keV HXR emission at 30% of the image's maximum. Note the *TRACE* white-light enhancement which coincides with the southern HXR footpoint observed by *RHESSI*.

in the integrated intensities of the He I and O V lines, indicating that the CDS slit is located on energized parts of the flare ribbons, as well as plasma downflows in the chromospheric and transition region layers (Figure 10). These downflows reach velocities up to about 20 km s^{-1} in He I and 30–40 km s^{-1} in O V. In the coronal Si XII line, we observe line-of-sight upflow velocities up to -50 km s^{-1}, starting at 08:22 UT and then developing gradually. Unfortunately, we do not have a hot flare line formed at temperatures around 10^7 K to study the behavior of the hottest component of the flaring plasma. The observed flow behavior (downflows in the chromosphere and lower transition region; upflows in coronal lines) is suggestive of explosive chromospheric evaporation. This is also supported by the strong HXR peaks at this time, which are due to nonthermal electrons impacting on the lower atmospheric layers from a coronal acceleration site, and the associated strong peaks in He I and O V.

We observe another distinct peak in *RHESSI* HXRs around 08:29 UT. At this time, the CDS slit is crossing the strongest energy deposition site along the southern flare ribbon, as is evidenced by the *RHESSI* 20–60 keV images as well as by the bright *TRACE* flare kernel within the spectrometer slit (see Figure 7). At this time, we also observe distinct peaks in the CDS O V intensity curves in the selected CDS pixels and strong upflows with velocities up to -100 km s^{-1} derived from the one-component Gaussian fits (Figure 10). However, in 8 pixels on the lower end of the CDS slit, we observe double components in the O V spectra roughly at this period (08:27:03

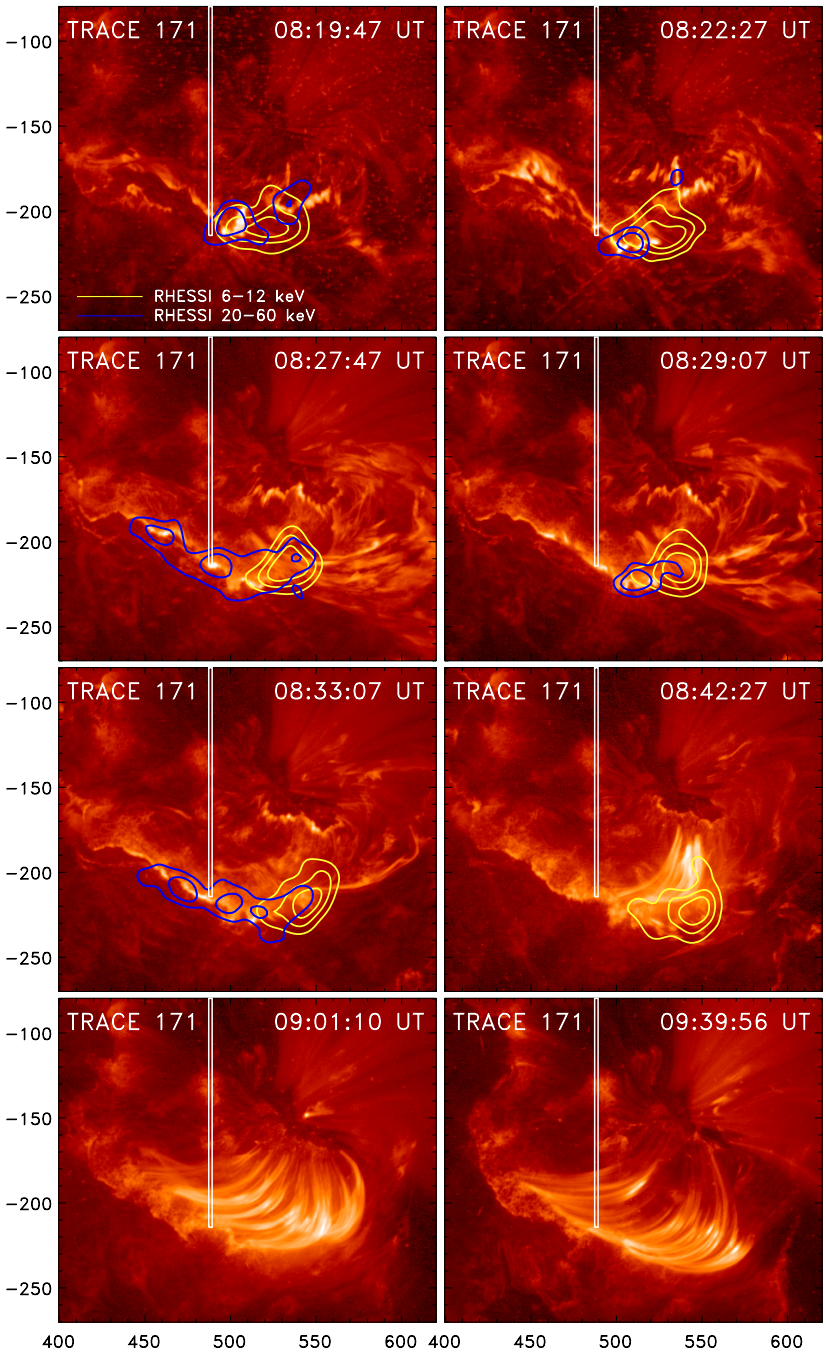

Figure 6. Sequence of *TRACE* 171 Å images together with contours of *RHESSI* 6–12 (yellow) and 20–60 keV (blue) images closest in time. Contour levels are 40%, 60%, and 80% of each image's maximum in the 6–12 keV energy range; 50% and 75% levels in the 20–60 keV range. At 08:45 UT, the *RHESSI* spacecraft entered the Earth shadow stopping the observations. The accompanying movie3 shows the flare evolution in *TRACE* 171 Å together with *RHESSI* 6–12 and 20–60 keV contours during the impulsive phase.

(An animation of this figure is available in the online journal.)

to 08:29:04 UT). In Figure 11, we show the evolution of O v spectra in three selected CDS pixels (the same pixels, for which we show the intensities and velocities in Figure 10) which change from single- to double-component spectra, together with the single-/double-component Gaussian fits. This spectral evolution is consistent with the bulk of the emission coming from a stationary plasma volume with an increasing contribution from upflowing plasma elements with velocities in the range of about −150 to −280 km s^{-1}. (The velocities of the first component lie all within the 3σ uncertainties, which we derived for the CDS O v one-component fits; these uncertainties are even larger for the double-component fits. Thus we interpret the velocity derived for this component as consistent with emission from a stationary plasma.) The upflow velocities obtained from the two-component fits are also plotted in Figure 10 together with the velocities derived from the one-component fits.

3.4. RHESSI X-ray Spectroscopy and Imaging

Figure 12 shows *RHESSI* X-ray spectra together with the thermal plus nonthermal fits accumulated during four selected

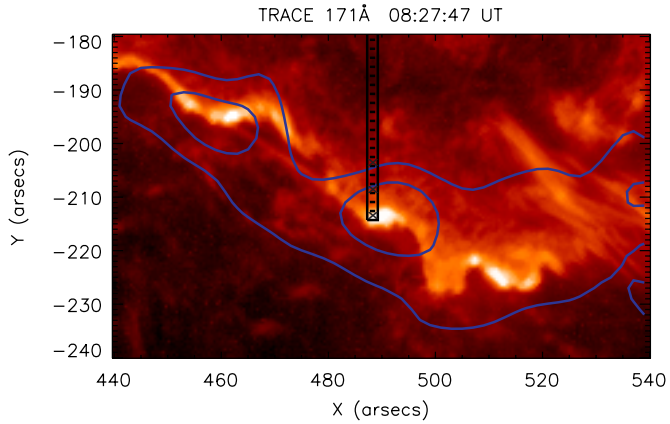

Figure 7. Small subfield of a *TRACE* 171 Å image (taken at 08:27:47 UT) together with contours of the *RHESSI* 20–60 keV image (blue) closest in time. The black rectangle shows the location of the CDS slit, indicating the size of the individual CDS pixels by the horizontal lines. Roughly 10 CDS pixels located at the bottom part of the slit are at some instant located along the flare ribbon (compare also Figure 6). The crosses mark those CDS pixels whose evolution is shown in Figures 8, 10, and 11.

peaks in the X-ray light curves (indicated by vertical lines in Figure 13). From these fits, we derive the temperature and emission measure of the hot flaring plasma as well as the spectral slope and power in electrons above a cutoff energy E_c for thick-target emission (Brown 1971). The observed *RHESSI* spectra (e.g., Figure 12) indicate that the emission $\gtrsim$20 keV is dominated by nonthermal power-law emission. This is also consistent with the (upper) estimates of E_c derived from the thick-target fits, which are in the range 15–25 keV. Therefore, in the following we use a fixed value of $E_c = 20$ keV to determine the kinetic energy of the fast electrons.

Figure 13 shows the time evolution of the plasma and electron beam parameters obtained from the fits to the *RHESSI* spectra integrated over consecutive 12 s intervals. From top to bottom we plot *RHESSI* X-ray light curves, plasma temperature, plasma emission measure, electron spectral index, and power in electrons for a low-energy cutoff $E_c = 20$ keV and for comparison also for $E_c = 35$ keV. The temperature peaks already at the first (small) HXR burst around 08:19 UT, with a maximum value of 23 MK. Emission measure is steeply growing until the largest

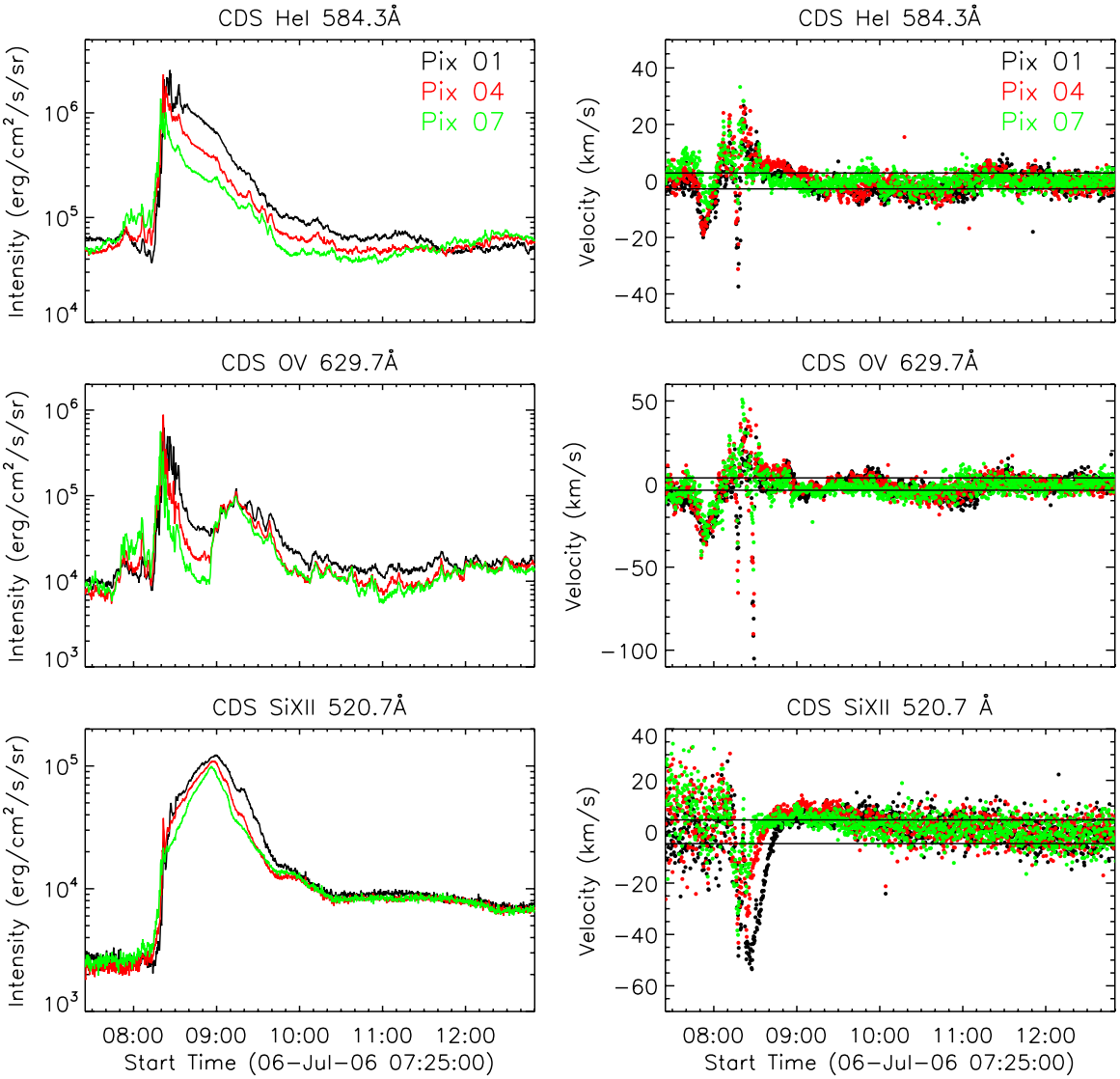

Figure 8. Evolution of integrated intensities (left: plotted on a logarithmic scale) and velocities (right) derived from the CDS spectral fits in He I, O V, and Si XII for the full CDS observation period in three different pixels along the lower end of the CDS slit (marked by crosses in Figure 7). Horizontal lines in the velocity curves indicate the 1σ uncertainties in the velocity calibration (derived during the postflare phase 11:00 to 12:55 UT).

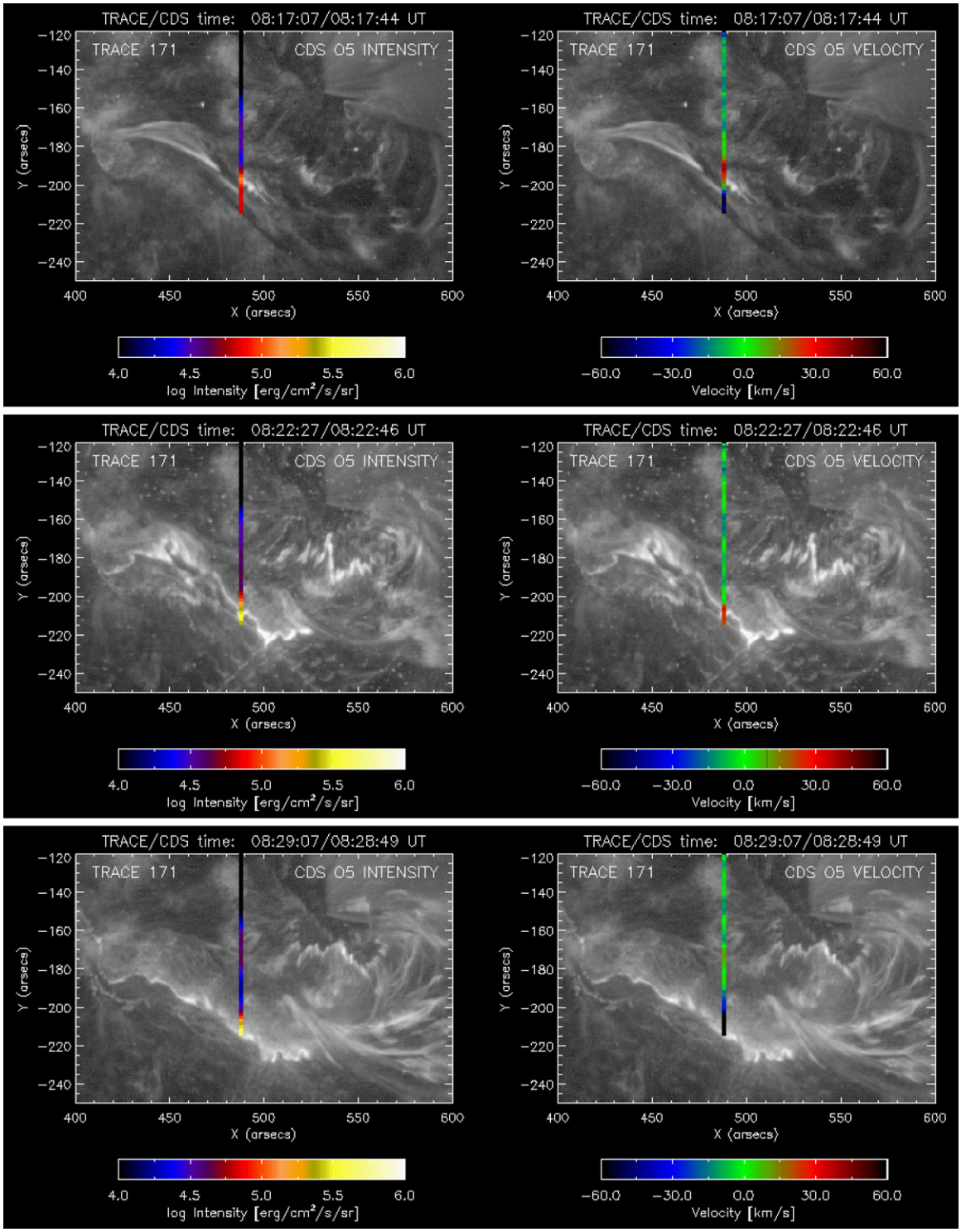

Figure 9. Three snapshots of *TRACE* 171 Å images combined with the integrated intensities (left) and velocities (right) derived from the Gaussian fit to a co-temporal CDS spectrum in the O v line. The top panel is taken during the time of the filament lift-off and commencement of the impulsive flare brightenings (the CDS velocities are blueshifted over the filament, and redshifted at the flare kernels), the middle panel around the time of the highest HXR peak (showing distinct redshifts at the CDS pixels crossing the flare ribbons), and the bottom panel during the time of the distinct late *RHESSI* peak associated with the strongest transition region upflows at the CDS pixels crossing the flare ribbons. The whole evolution is shown in the accompanying movie4 (note that only each second CDS spectrum available is plotted in the movie).

(An animation of this figure is available in the online journal.)

HXR peak at 08:23 UT and then gradually increasing beyond the end of the enhanced *RHESSI* HXR emission. Such behavior of emission measure and temperature indicates that first a small volume of coronal plasma is heated to high temperatures, and subsequently more and more loops are filled with hot plasma. The electron spectra are comparatively steep, with the spectrum being hardest at the time of the largest *RHESSI* peak at 08:23 UT with an electron spectral index $\delta \sim 4.5$.

In order to obtain the energy flux density in fast electrons, we also need the cross-sectional area of the electron beam,

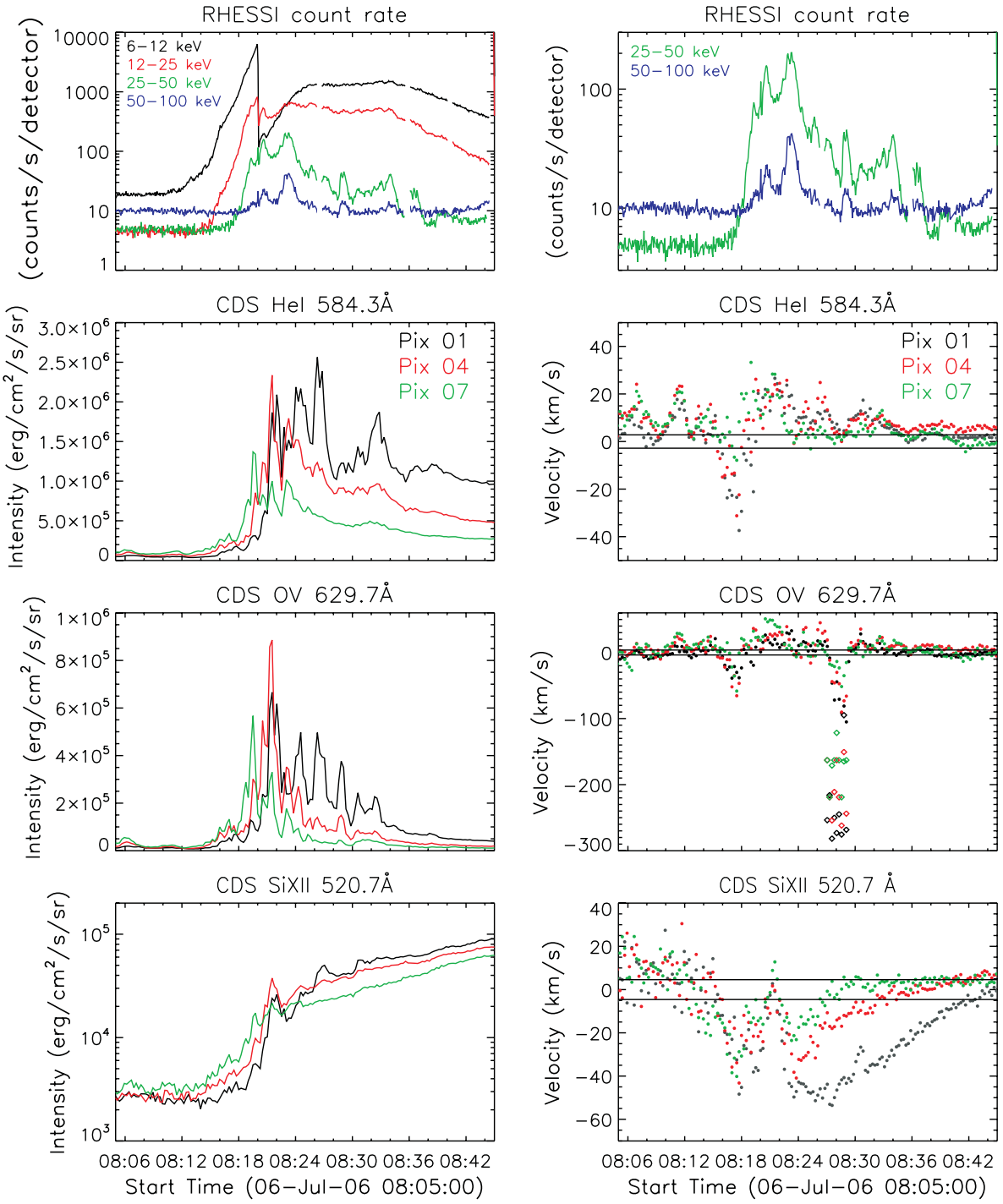

Figure 10. Flare impulsive phase. First row: *RHESSI* X-ray flux at several energy bands from 6 to 100 keV. (The discontinuity at the low energy bands at 08:20 UT is an artifact due to the change in the *RHESSI* attenuator state from A0 to A1.) Second to fourth row: evolution of integrated intensities (left) and velocities (right) derived from the one-component Gaussian fits to the He I, O V, and Si XII CDS spectra during the flare impulsive phase in three different pixels along the lower end of the CDS slit (marked by crosses in Figure 7). Horizontal lines in the velocity curves indicate the 1σ uncertainties in the velocity calibration. For the O V line, we also plot the velocities derived from the two-component fits during the period 08:27–08:29 UT (indicated by triangles). Note that the He I and O V intensities are plotted on a linear scale, to make the bursty nature clearer, whereas in Figure 8 they are plotted logarithmically.

which we estimate from the HXR sources. HXR footpoint sizes were determined from *RHESSI* images reconstructed over individual peaks in the 20–60 keV band using the Pixon and the MEM-NJIT algorithms. For the highest *RHESSI* peak during 08:22–08:24 UT the derived area is in the range $A \sim (2\text{–}4) \times 10^{17}$ cm^2, and for the small peak during around 08:29 UT, which is accompanied by the highest upflow velocities observed by CDS in the O V line, we find $A \sim (4\text{–}8) \times 10^{17}$ cm^2. The uncertainties of about a factor of 2 were obtained from the different image reconstruction algorithms. In Figure 14, we show the two *RHESSI* Pixon images that we used for the source size determination.

With the energy flux in electrons above 20 keV obtained from the *RHESSI* spectral fits (see Figure 13), this gives for the highest

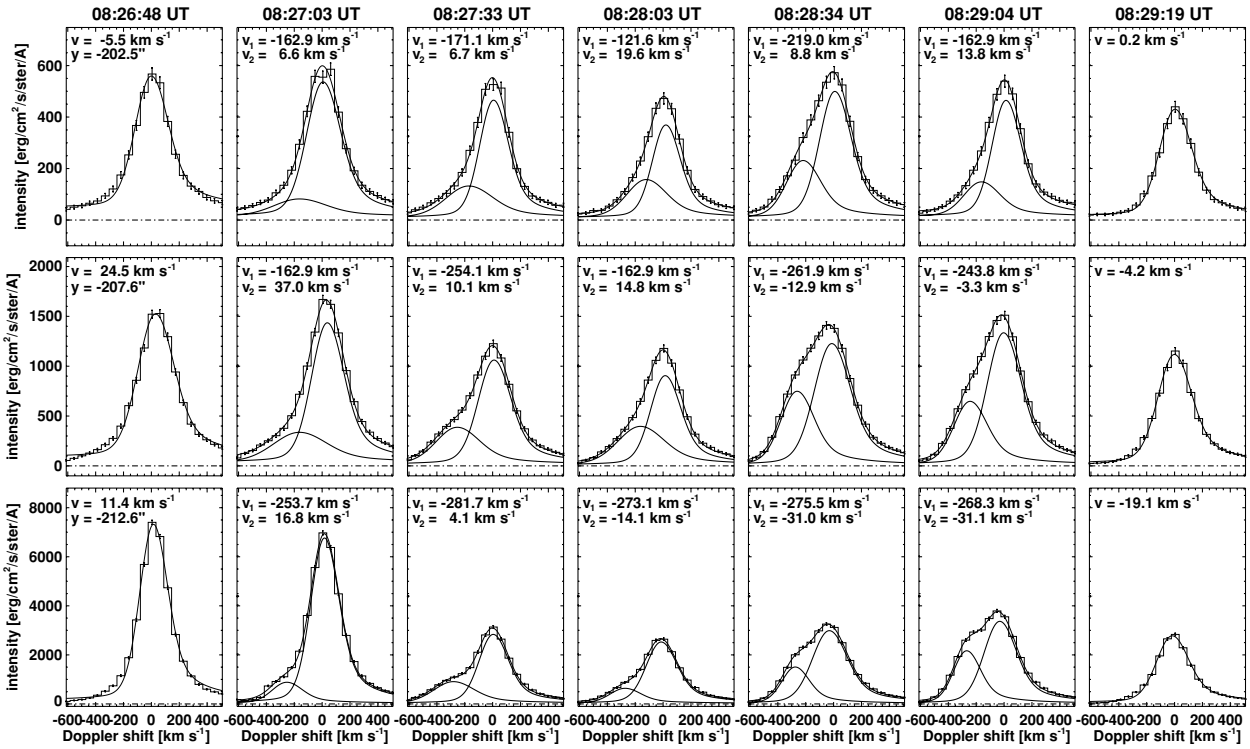

Figure 11. Sequence of O v spectra during the flare peak, fitted with a double component (except for the first and last spectrum of the series) for three pixels along the lower end of the CDS slit (marked by crosses in Figure 7). Only each second spectrum available in the time series is plotted.

RHESSI peak during 08:22–08:24 UT an energy flux density of $P_{20} = (4–7) \times 10^{10}$ erg s $^{-1}$ cm^{-2}, and for the peak at 08:29 UT $P_{20} = (3–5) \times 10^{9}$ erg s $^{-1}$ cm^{-2}.

4. DISCUSSION

The comparison of the energy flux densities in electrons that we derived from the *RHESSI* observations with the results of hydrodynamic simulations of the atmospheric response to electron beam heating (e.g., Nagai & Emslie 1984; Fisher et al. 1985a, 1985b, 1985c; Abbett & Hawley 1999b; Allred et al. 2005) suggests that for the largest *RHESSI* peak during 08:22–08:24 UT the derived value of $P_{20} = (4–7) \times 10^{10}$ erg s $^{-1}$ cm^{-2} is consistent with explosive chromospheric evaporation. Fisher et al. (1985c) estimated from their simulations a threshold between gentle and explosive evaporation of $P_{20} \sim 10^{10}$ erg s $^{-1}$ cm^{-2}. The CDS measurements during this period show downflows in the range 20–40 km s^{-1} in the "cool" lines formed in the chromosphere and transition region, while we observe upflows with line-of-sight velocities up to about -50 km s^{-1} in the hot coronal Si XII line (Figure 10). This flow behavior in the different layers of the flaring atmosphere matches qualitatively the expectations for explosive chromospheric evaporation. During the explosive evaporation process, strong pressure gradients build up in the chromosphere/lower transition region driving plasma flows in both directions. Due to the larger mass and inertia of the chromosphere, the downflows are slower than the upflows of the hot plasma, establishing momentum balance. The characteristics of the transition region lines that we observed during this highest peak is in line with the results of Kamio et al. (2005), who detected short-lived O v transition region downflows at the locations of Hα flare kernels at the time of the strongest energy input (as evidenced by the peak of the GOES SXR flux derivative) in all four flares of their study. In addition, these authors report that the intermediate temperature between chromospheric evaporation upflows and downflows is close to Mg IX (1.0 MK).

The relatively small upflow velocities observed in the Si XII line ($T \sim 2 \times 10^6$ K) are basically in line with the recent hydrodynamic simulations by Liu et al. (2009), who calculated the relation of the plasma flow velocities and the temperature. However, *TRACE* postflare loops (see the last two panels in Figure 6) indicate that the loop geometry relative to the CDS slit is actually not very favorable to measure line-of-sight velocities in the corona, since the coronal loops cross the slit with a strong transversal component, and the coronal velocities derived from the Si XII line may be underestimated. We also note that the intensity behavior in the Si XII line (impulsive emission spike followed by a gradual increase, i.e., a kind of Neupert-effect-type plasma response; see Figure 10, bottom panels) indicates that we observe the emission of plasma accumulating in the corona along the line of sight in the selected CDS pixels, due to the chromospheric evaporation process. This is quite different from the impulsive peaks observed in He I and in O v (Figure 10, middle panels), where we observe the emission from narrow layers in the chromosphere and transition region, and the intensity increase occurs instantaneously and correlated with the energy input sequence.

More interesting because difficult to reconcile with the "simple" explosive versus gentle evaporation picture is the plasma behavior when compared to the electron beam parameters derived for the small but distinct HXR burst at 08:29 UT. For the energy flux density in electrons we find $P_{20} = (3–5) \times 10^9$ erg s^{-1} cm^{-2}, which is a heating flux too small to drive explosive chromospheric evaporation according to the model results of Fisher et al. (1985c). This would suggest that gentle chromospheric evaporation is at work, and the transition region is expected to slowly ablate with velocities of the order of some ten km s^{-1}. However, at that period we observe the highest upflow velocity in the O v transition region line during the event,

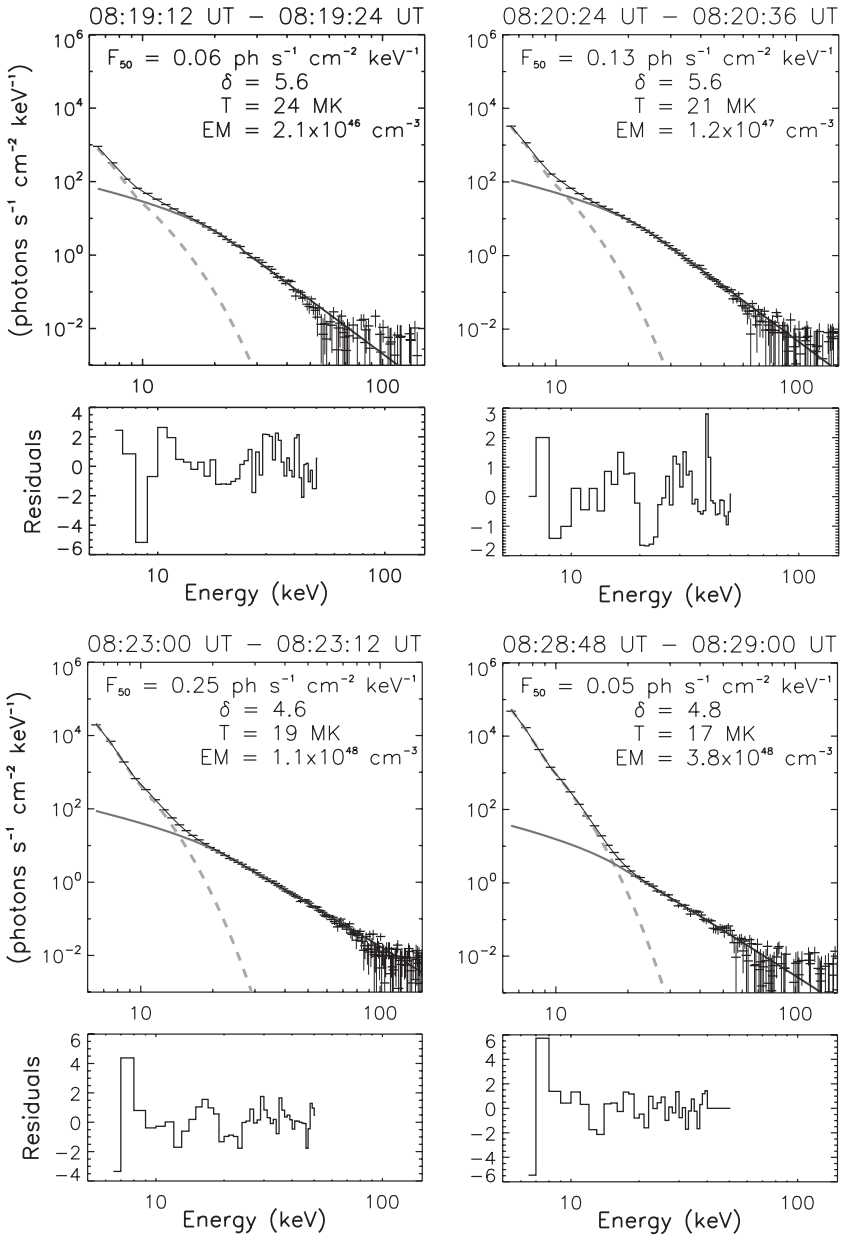

Figure 12. *RHESSI* X-ray spectra accumulated during four selected peaks in the *RHESSI* HXR light curves (indicated in the time series in Figure 13). The top panels show the observed X-ray spectra together with the two-component fits consisting of the bremsstrahlung and line emission of an isothermal plasma (dominating at low energies) plus the nonthermal thick-target bremsstrahlung emission of a power-law electron distribution with a low-energy cutoff (dominating at high energies, $\gtrsim$20 keV). The fit parameters derived are annotated in the spectrum plots. The bottom panels show the fit residuals (i.e., the difference between the observed counts and the model predicted counts divided by the estimated 1σ uncertainty in the counts) in the fit range.

with line-of-sight velocities up to -280 km s^{-1}. We note that we cannot exclude the possibility that the power in the electron beam is actually higher than we derived in our analysis, since this quantity critically depends on the cross-sectional area of the HXR footpoints and the low-energy cutoff to the accelerated electron spectrum, which are both difficult to exactly derive from the observations. The value we derived for the energy flux in electrons is actually close to the threshold between gentle and explosive evaporation. However, even in the case that the energy flux in electrons would indeed suffice to drive explosive chromospheric evaporation, the CDS observations cannot straightforwardly be reconciled with the hydrodynamic modeling results of the flaring atmosphere in terms of explosive versus gentle evaporation because the velocity of 280 km s^{-1} in the O v transition region line is directed upward. It is also considerably higher than the upper limit derived by Fisher et al. (1985b) for the expansion velocity of explosive chromospheric evaporation, which is about 2.35 times the sound speed of the evaporating plasma. The formation temperature of the O v spectral line is 2.7×10^5 K and the corresponding sound speed $\sim$70 km s^{-1}, giving a limit to the expansion velocity of about 140 km s^{-1}.

We also stress that during these times, we observe in the O v transition region line contributions from both a stationary and a high-velocity upflowing plasma volume, in single CDS pixels which have a size as small as $2'' \times 1\farcs7$, corresponding to an area of 1.8×10^{16} cm^2. This implies intriguing dynamics on fine-structured scales of the flaring atmosphere. Double-component spectra in transition region lines during a flare have been observed before in individual pixels during high-cadence CDS sit-and-stare spectroscopic observing mode (Brosius 2003)

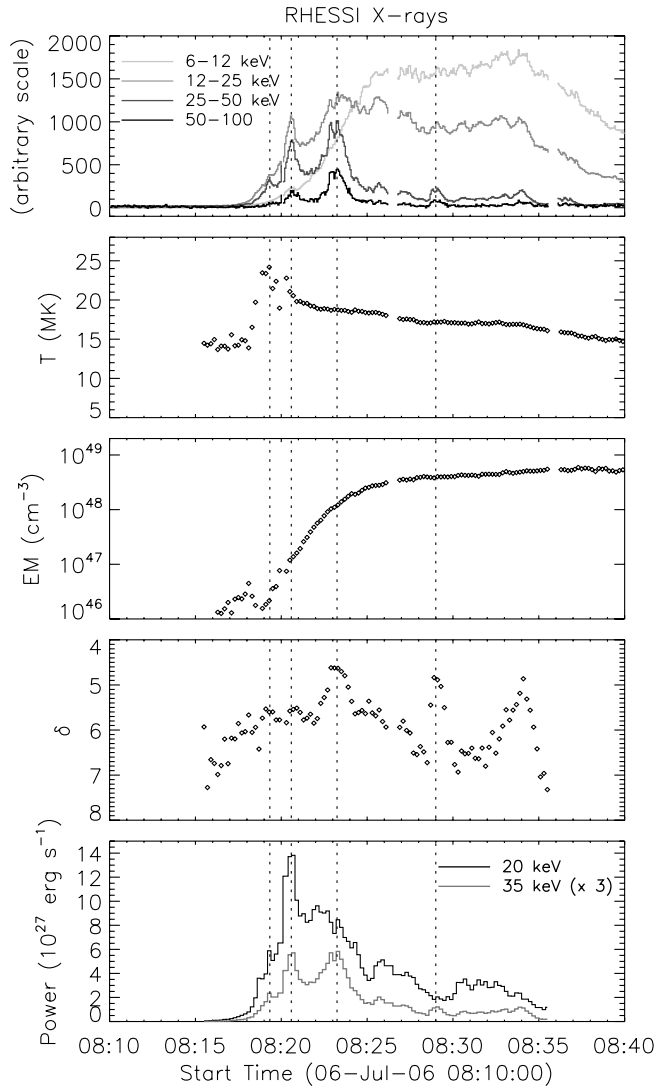

Figure 13. Time evolution of the thermal plasma parameters and nonthermal electron beam parameters derived from *RHESSI* X-ray spectral fits of consecutive 12 s integration intervals. From top to bottom: corrected *RHESSI* count rates in different energy bands (the scales in the different energy bands are altered in order to better see the time evolution), plasma temperature, emission measure, electron spectral index δ, and power in electrons derived for thick-target emission with cutoff energies of 20 keV and 35 keV, respectively. The vertical lines denote the time of the spectra plotted in Figure 12.

but—at least to our knowledge—have not been reported and studied in detail in spectra rastering over the flare region. This is most probably due to the very dynamic nature of the transition region during solar flares, which is difficult to capture in raster mode. It is also remarkable that this distinct intensity peak showing high upflow velocities in the O v transition region line is not accompanied by an intensity peak or plasma flows in the chromospheric He I line. This suggests that most of the electron beam energy is deposited in the transition region layers causing the strong plasma upflows there, and does not reach the chromosphere.

Finally, we note that the light curves extracted in individual CDS pixels in the He I and O v spectral lines show several distinct peaks during the impulsive flare evolution. This implies that either (1) the same area of the solar atmosphere is energized several times during the event (which is in conflict with the standard eruptive flare model, where magnetic reconnection driven by the erupting CME activates in sequence different magnetic loops further and further away from the magnetic inversion line), or (2) different loops are energized within the same pixel (multi-thread scenario) but cannot be distinguished within the spatial resolution of the instruments. The multi-thread interpretation could also explain the double-component spectra observed in individual CDS pixels. In addition, in the multi-thread scenario the electron beam flux on individual threads would be larger than we estimated, and could potentially explain the large range of upflow velocities that is observed with each HXR burst.

5. CONCLUSIONS

We presented high-cadence CDS spectroscopy combined with high-cadence imaging of the solar atmosphere in comparison with the energy input by fast electrons as derived from *RHESSI* HXRs in an M2.5 flare. For the flare impulsive phase, the plasma flow behavior (simultaneous downflows in the "cool" He I and O v lines formed in the chromosphere and transition region, and upflows in the hot coronal Si XII line) as well as the derived energy deposition rate by electron beams are consistent with explosive chromospheric evaporation. However, for a later distinct HXR burst, where the strongest energy deposition site is exactly located on the CDS slit, the situation is much more complex. The energy input by electrons is about an order of magnitude smaller than during the flare peak and too small

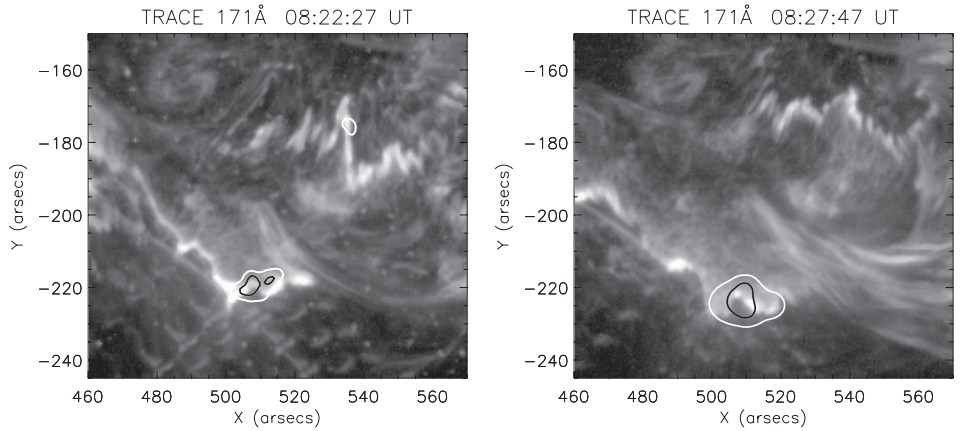

Figure 14. *TRACE* 171 Å filtergrams and overlay of *RHESSI* 20–60 keV images reconstructed with the Pixon algorithm during two distinct HXR peaks associated with strong chromospheric evaporation flows. The *RHESSI* image integration times are 08:22:48–08:23:36 UT (left) and 08:28:30–08:30:00 UT (right). The contours are at the 30% (white) and 50% (black) levels of each image's maximum. Note that the *RHESSI* flare area used to determine the electron beam flux was derived within the 50% contour of these images.

to drive explosive chromospheric evaporation. However, at the same time we observe the highest upflow velocities in the O v transition region line during the event, up to 280 km s^{-1}, in addition to the contribution of a stationary plasma component within the same CDS pixel. The upflow velocities are much too high for gentle ablation of the transition region. These findings indicate that the flaring transition region is extremely dynamic, complex, and fine structured on scales that are smaller than can be resolved with present instrumentation, and is thus probably not adequately captured by single-loop hydrodynamic simulations of the flaring atmosphere.

A.M.V. gratefully acknowledges support of the Austrian Science Fund (FWF): P20867-N16. M.T. is a recipient of an APART-fellowship of the Austrian Academy of Sciences at the Institute of Physics, University of Graz (APART 11262). This work was supported by the scientific exchange program SK-AT-0004-08 of the "Österreichischer Austauschdienst" ÖAD (Austria) and the Slovak Research and Development Agency SRDA (Slovakia) as well as by the SRDA project APVV-0066-06. Data were acquired in the frame of the *SOHO* Joint Observing Program JOP171 operated in cooperation with the *TRACE* satellite, the *SOHO* satellite, and the ground-based DOT, Hvar, and Kanzelhöhe telescopes. The authors are grateful for the cooperation of the *SOHO*, *TRACE*, and DOT teams during the run of JOP171 in 2006 July. *SOHO* is a project of international cooperation between ESA and NASA. *TRACE* is a mission of the Stanford-Lockheed Institute for Space Research and part of the NASA Small Explorer Mission. *RHESSI* is a NASA small explorer mission. A.M.V. thanks Luca Teriaca, Ryan Milligan, Wei Liu, and Ken Phillips for interesting and insightful discussions. We are also grateful to the anonymous referee for his/her insightful comments which helped to improve the paper.

REFERENCES

Abbett, W. P., & Hawley, S. L. 1999a, ApJ, 521, 906
Abbett, W. P., & Hawley, S. L. 1999b, ApJ, 521, 906
Allred, J. C., Hawley, S. L., Abbett, W. P., & Carlsson, M. 2005, ApJ, 630, 573
Antonucci, E., et al. 1982, Sol. Phys., 78, 107
Attrill, G. D. R., van Driel-Gesztelyi, L., Démoulin, P., Zhukov, A. N., Steed, K., Harra, L. K., Mandrini, C. H., & Linker, J. 2008, Sol. Phys., 252, 349
Bentley, R. D., Doschek, G. A., Simnett, G. M., Rilee, M. L., Mariska, J. T., Culhane, J. L., Kosugi, T., & Watanabe, T. 1994, ApJ, 421, L55
Berkebile-Stoiser, S., Gömöry, P., Veronig, A. M., Rybák, J., & Sütterlin, P. 2009, A&A, 505, 811
Brosius, J. W. 2003, ApJ, 586, 1417
Brosius, J. W. 2009, ApJ, 701, 1209
Brosius, J. W., & Phillips, K. J. H. 2004, ApJ, 613, 580
Brown, J. C. 1971, Sol. Phys., 18, 489
Canfield, R. C., Metcalf, T. R., Zarro, D. M., & Lemen, J. R. 1990, ApJ, 348, 333
Culhane, J. L., et al. 1993, Adv. Space Res., 13, 303
Czaykowska, A., de Pontieu, B., Alexander, D., & Rank, G. 1999, ApJ, 521, L75
Del Zanna, G. D., Schmieder, B., Mason, H., Berlicki, A., & Bradshaw, S. 2006, Sol. Phys., 239, 173
Delaboudinière, J.-P., et al. 1995, Sol. Phys., 162, 291
Dennis, B. R., & Pernak, R. L. 2009, ApJ, 698, 2131
Dennis, B. R., & Zarro, D. M. 1993, Sol. Phys., 146, 177
Domingo, V., Fleck, B., & Poland, A. I. 1995, Sol. Phys., 162, 1
Doschek, G. A. 1990, ApJS, 73, 117
Doschek, G. A., Feldman, U., Kreplin, R. W., & Cohen, L. 1980, ApJ, 239, 725
Doschek, G. A., & Warren, H. P. 2005, ApJ, 629, 1150
Fisher, G. H., Canfield, R. C., & McClymont, A. N. 1985a, ApJ, 289, 434
Fisher, G. H., Canfield, R. C., & McClymont, A. N. 1985b, ApJ, 289, 425
Fisher, G. H., Canfield, R. C., & McClymont, A. N. 1985c, ApJ, 289, 414
Hammerschlag, R. H., & Bettonvil, F. C. M. 1998, New Astron. Rev., 42, 485
Handy, B. N., et al. 1999, Sol. Phys., 187, 229
Harrison, R. A., et al. 1995, Sol. Phys., 162, 233
Holman, G. D., Sui, L., Schwartz, R. A., & Emslie, A. G. 2003, ApJ, 595, L97
Hori, K., Yokoyama, T., Kosugi, T., & Shibata, K. 1997, ApJ, 489, 426
Hudson, H. S., Acton, L. W., & Freeland, S. L. 1996, ApJ, 470, 629
Hurford, G. J., et al. 2002, Sol. Phys., 210, 61
Jiang, Y., Yang, L., Li, K., & Ren, D. 2007, ApJ, 662, L131
Kamio, S., Kurokawa, H., Brooks, D. H., Kitai, R., & UeNo, S. 2005, ApJ, 625, 1027
Landini, M., & Monsignori Fossi, B. C. 1990, A&AS, 82, 229
Leka, K. D. 1997, ApJ, 484, 900
Lin, R. P., & Hudson, H. S. 1976, Sol. Phys., 50, 153
Lin, R. P., et al. 2002, Sol. Phys., 210, 3
Liu, W., Petrosian, V., & Mariska, J. T. 2009, ApJ, 702, 1553
MacNeice, P., Burgess, A., McWhirter, R. W. P., & Spicer, D. S. 1984, Sol. Phys., 90, 357
Mariska, J. T., Doschek, G. A., & Bentley, R. D. 1993, ApJ, 419, 418
Mariska, J. T., Emslie, A. G., & Li, P. 1989, ApJ, 341, 1067
McIntosh, S. W., Leamon, R. J., Davey, A. R., & Wills-Davey, M. J. 2007, ApJ, 660, 1653
Milligan, R. O., & Dennis, B. R. 2009, ApJ, 699, 968
Milligan, R. O., Gallagher, P. T., Mathioudakis, M., Bloomfield, D. S., Keenan, F. P., & Schwartz, R. A. 2006a, ApJ, 638, L117
Milligan, R. O., Gallagher, P. T., Mathioudakis, M., & Keenan, F. P. 2006b, ApJ, 642, L169
Nagai, F., & Emslie, A. G. 1984, ApJ, 279, 896
Neupert, W. M. 1968, ApJ, 153, L59
Otruba, W. 2005, Hvar Obs. Bull., 29, 279
Otruba, W., & Pötzi, W. 2003, Hvar Obs. Bull., 27, 189
Pauluhn, A., et al. 1999, Appl. Opt., 38, 7035
Qiu, J., Lee, J., Gary, D. E., & Wang, H. 2002, ApJ, 565, 1335
Rüedi, I., Solanki, S. K., & Livingston, W. 1995, A&A, 302, 543
Scherrer, P. H., et al. 1995, Sol. Phys., 162, 129
Schwartz, R. A., Csillaghy, A., Tolbert, A. K., Hurford, G. J., McTiernan, J., & Zarro, D. 2002, Sol. Phys., 210, 165
Shimizu, T., et al. 2009, ApJ, 696, L66
Smith, D. M., et al. 2002, Sol. Phys., 210, 33
Stucki, K., Solanki, S. K., Pike, C. D., Schühle, U., Rüedi, I., Pauluhn, A., & Brković, A. 2002, A&A, 381, 653
Temmer, M., Veronig, A. M., Vršnak, B., Rybák, J., Gömöry, P., Stoiser, S., & Maričić, D. 2008, ApJ, 673, L95
Teriaca, L., Falchi, A., Cauzzi, G., Falciani, R., Smaldone, L. A., & Andretta, V. 2003, ApJ, 588, 596
Teriaca, L., Falchi, A., Falciani, R., Cauzzi, G., & Maltagliati, L. 2006, A&A, 455, 1123
Veronig, A., Vršnak, B., Dennis, B. R., Temmer, M., Hanslmeier, A., & Magdalenić, J. 2002, A&A, 392, 699
Vršnak, B., Temmer, M., Veronig, A., Karlický, M., & Lin, J. 2006, Sol. Phys., 234, 273
Warren, H. P., & Doschek, G. A. 2005, ApJ, 618, L157
Wuelser, J., et al. 1994, ApJ, 424, 459
Zarro, D. M., Canfield, R. C., Metcalf, T. R., & Strong, K. T. 1988, ApJ, 324, 582
Zarro, D. M., Sterling, A. C., Thompson, B. J., Hudson, H. S., & Nitta, N. 1999, ApJ, 520, L139